



Article

Modeling De-Coring Tools with Coupled Multibody Simulation and Finite Element Analysis

Melvin Mariadass ^{1,*}, Roman Binder ¹ , Florian Etemeyer ², Wolfram Volk ^{2,3} and Daniel Günther ²¹ Fill Gesellschaft m.b.H., Fillstraße 1, 4942 Gurten, Austria; roman.binder@fill.co.at² Fraunhofer Research Institution for Casting, Composite and Processing Technology IGCV, Lichtenbergstrasse 15, 85748 Garching, Germany; florian.ettemeyer@mytum.de (F.E.); wolfram.volk@utg.de (W.V.); daniel.guenther@igcv.fraunhofer.de (D.G.)³ Chair of Metal Forming and Casting, Technical University of Munich, Walther-Meissner-Strasse 4, 85748 Garching, Germany

* Correspondence: melvin.mariadass@fill.co.at

Abstract: De-coring is an essential process in the casting process chain, determining the quality and cost of production. In this study, a coupled multibody system (MBS) and finite element modeling (FEM) technique is presented to study the mechanical loads during the de-coring process. The removal of cast-in sand cores from the inner regions of the cast part by de-coring or knocking out is a complex process with dynamic loads. Currently, the process relies upon empirical knowledge and tests. Inorganic sand cores pose additional challenges in the success of the de-coring process. Increasing complexity in geometry and stringent environmental regulations compel a predictive process in the earlier stages of design. Predicting the process' success is challenged by the dynamic non-linearities of the system. The dynamic characteristics and the interaction between hammer and casting were studied here for the first time using an industrial-based test rig, and a novel modeling approach was formulated. The results of the developed model are in good compliance with the experiments. The methodology presented in this study can be used to include a varying number of hammers and loads. The proposed approach presents the possibility to discretize the process and qualitatively assess the process parameters for optimization.

Keywords: de-coring process; inorganic sand binder; finite element modeling; multibody system; flexible coupled simulation; non-linear; process dynamics



Citation: Mariadass, M.; Binder, R.; Etemeyer, F.; Volk, W.; Günther, D. Modeling De-Coring Tools with Coupled Multibody Simulation and Finite Element Analysis. *Appl. Mech.* **2023**, *4*, 1206–1226. <https://doi.org/10.3390/applmech4040062>

Received: 18 October 2023
Revised: 20 November 2023
Accepted: 21 November 2023
Published: 6 December 2023



Copyright: © 2023 by the authors. Licensee MDPI, Basel, Switzerland. This article is an open access article distributed under the terms and conditions of the Creative Commons Attribution (CC BY) license (<https://creativecommons.org/licenses/by/4.0/>).

1. Introduction

The production of detailed interior cavities of iron or aluminum is possible using sand casting methods. Sand cores bonded using organic or inorganic binders shape the hollow regions of a casting and are removed once cast. Sand cores are produced using core shooting or 3D printing technology. They must offer structural and thermal stability to retain their shape before casting while easily disintegrating after casting.

1.1. Casting Inorganics

Application of inorganic binders in the production of sand cores is preferred due to their environmentally friendly properties. However, inorganic binders lack the favorable de-coring properties offered by organic binders [1]. Increasing environmental concern and emission controls have resulted in the use of odorless and emission-free inorganic binders being favored [2].

1.2. De-Coring Process

Industrially, sand cores are removed from casting cavities through mechanical load and agitation [1], referred to as knocking out or de-coring. The process of de-coring a cast part removes the inner sand core while leaving the cast section itself unharmed. De-coring

behavior is mainly attributed to the design of the casting, especially the number and size of openings, type of sand, and binder system; furthermore, hardening the core via baking, exposing the sand core to more heat, and selecting suitable de-coring equipment enhances the process [3].

Unlike organic sand cores, thermal stresses reached during aluminum casting are not sufficient to break the inorganic sand core, thereby requiring external effort. Currently, the de-coring process is empirically determined for each casting due to inadequate virtual descriptions of the de-coring process.

1.3. Material Behavior

Stauder et al. studied the de-coring properties of sand cores for different sand binders and thermal history and parameterized the material parameters in accordance with the Mohr–Coulomb failure criterion [4–7]. He also quantified the de-coring properties of sand cores based on residual strength and de-agglomeration rate. Core properties are locally altered by the transient overlay of mechanical and thermal loads. In addition, thermal stability and ambient conditions adversely affect the removal of inorganically bonded sand cores [4]. The mechanical properties of inorganic sand cores vary locally due to in-homogeneous structures and the influence of production parameters [8]. Dong et al. described shell mold cracking by relating fracture stress and effective volume using Weibull’s statistical method as a criterion to evaluate the strength of brittle materials [9]. Further, Lechner proposed a novel weakest-link-based Mohr–Coulomb failure criterion to predict the fracture strength of inorganic sand cores [10]. Ettemeyer et al. characterized the de-coring properties of inorganic sand cores and described the behavior using the Drucker–Prager yield criterion [11].

1.4. Investigation via Knocking out

The process of removing the sand core via mechanical agitation is governed by several parameters. A bob knock-out test is performed to quantify the de-coring using total impact energy [1]. The casting geometry and size of the openings dominate the process towards the end [5]. The effect of load intensities on the removal rate of cores is significant in predicting the removal process [4]. Additionally, the internal friction and compression strength of cast-in sand cores were identified as vital for de-coring [11]. Machine learning models were trained to identify significant parameters for the de-coring process [12].

These pioneering studies determined the fundamental characteristics of sand cores that result in better core removal properties. A high force and frequency of impulse is suggested to enhance the material removal rate [1,5]. However, a meticulous investigation on the interaction between hammer and casting is not present in this study. The distribution of cyclic dynamic loads on the casting is critical in understanding the fracture regions. Furthermore, the positional placement of the load to initiate fracturing and the material for fixture are particularly significant for complex and filigree sand core geometries. The characterization of de-coring devices is crucial in advancing knowledge of the process.

1.5. Simulation of FEM–MBS Coupling

The dynamic forces during the described process are investigated for the first time in this work. The experimental test rig is an industrial de-coring machine from the Fill Gesellschaft, m.b.H., Gurten, Austria, equipped with a POLYTEC CLV 2534 Laser Doppler Vibrometer (LDV), Polytec GmbH, Waldbronn, Germany. The specimens cast for the experiment were de-cored on the hammer station using a de-coring hammer, OMLER AF1470 MBL, OMERL s.r.l, Bandito CN, Italy. Additionally, a novel numerical approach is proposed to formulate the process. This approach benefits from the coupled FEM–MBS technique when studying the mechanical loads present throughout the process.

The de-coring hammer considered in this study is primarily a pneumatic hammer with a telescopic cylinder and a reciprocating piston inside the cylinder. A detailed mathematical model involving a non-linear valve area for a double-acting pneumatic cylinder was

developed by Richer [13]. The impact energy of air chisel hammers was studied using the rebound co-efficient and was validated [14]. A linear viscoelastic model for calculating impact stiffness has been postulated [15].

A flexible coupled multibody system offers the combined advantage of multi-body simulation and finite element analysis [16,17]. The contact forces due to rigid body movements were coupled with FEM model to analyze the force and deformation in the process. A reduced-order method was successfully implemented to study the mechatronic control systems of machine tool dynamics [18]. Analyzing combined structural properties of an experimentally identified model coupled to a simulated model is possible using dynamic substructuring [19].

The mathematical formulation for coupled flexible body simulation is detailed in this paper, and the process dynamic is characterized for the first time. The results convey acceptable agreement with measurements. The characteristics of the hammer and casting are quantified, and the time-varied impact energy delivered to the casting can be determined using this approach.

2. Materials and Methods

2.1. Casting

Hollow aluminum with a sand core was cast into the form of a bending beam (depicted in Figure 1). This allows ease of measurement and provides direct comparison possibility with existing research data. The production method and materials are elaborately discussed by Ettemeyer [11]. The cast specimen D from the work of Ettemeyer provides the basis for the samples utilized in this work. The sand core specimen has dimensions of 22.4 mm × 22.4 mm × 170 mm, made from silica sand that was H32-bonded using a 1.9% HA Cordis[®]-model binder (Hüttenes-Albertus Chemische Werke GmbH, Düsseldorf, Germany). The part was cast using an aluminum alloy (AlSi7Mg) at 750 °C in all specimens.

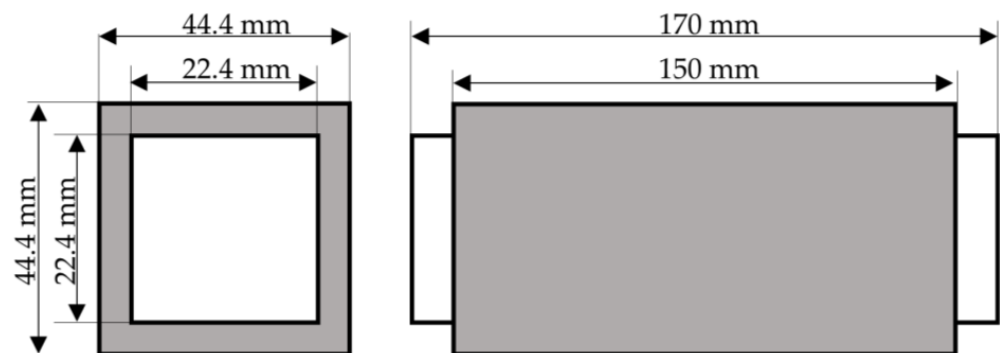


Figure 1. Sand core and casting specimen.

2.2. De-Coring Machine

An industrial de-coring machine from Fill GmbH mounted with a single OMLER AF1470-MBL pneumatic hammer serves for experimentation and validation. The pneumatic hammer has a two-stage working principle, as illustrated in Figure 2. The cylinder, which envelops a spool valve and inner piston, is mounted with a chisel. The cylinder is suspended by springs inside the housing and extends outwards. The casting is placed under the hammer at a distance.

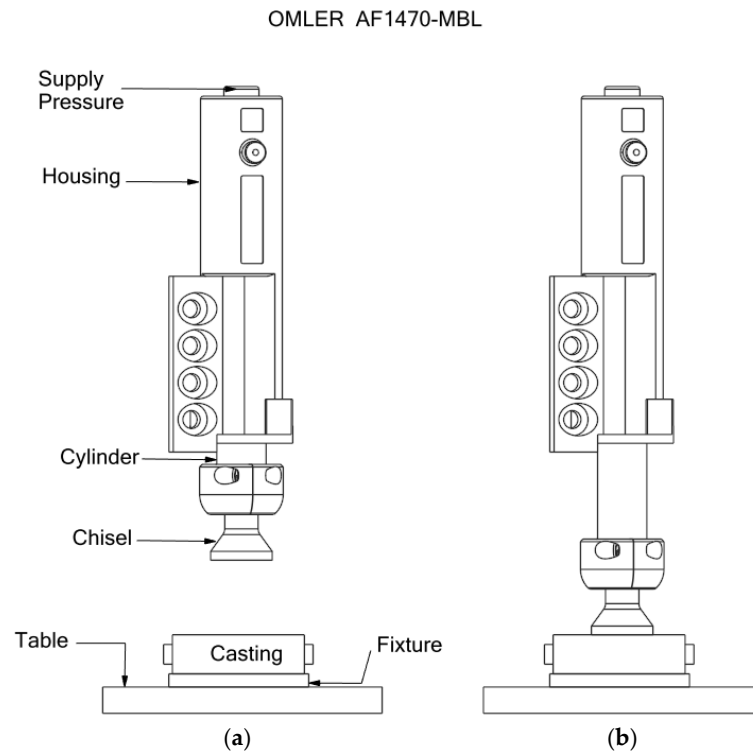


Figure 2. De-coring hammer (a) at rest and (b) in the working stage.

Upon supplying pressurized air to the hammer, the cylinder extends until chisel contacts the casting. The top cylinder chamber remains pressurized during the knocking-out process, pressing the chisel against the casting. The inner piston chamber is pressurized to start the percussion mechanism. The hammer is mounted to a machine station for stability, and the casting is fixed to the machine table. The machine table mounted with the hammer and casting is shown in Figure 3.

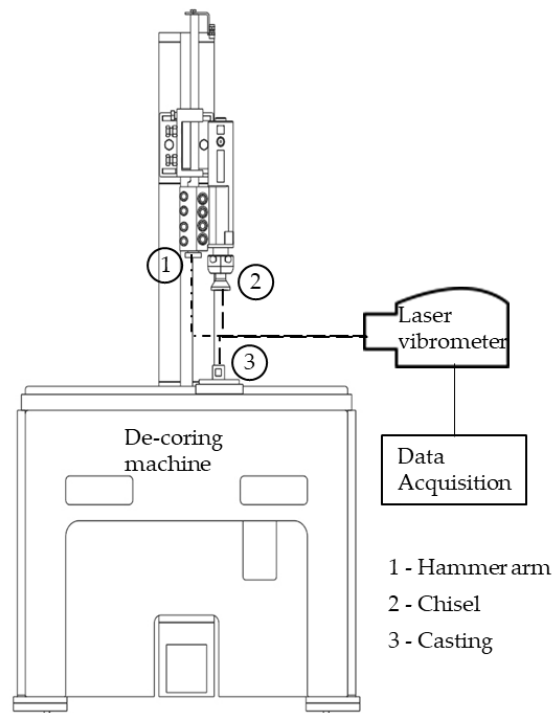


Figure 3. Hammer station and measurement points.

2.3. Experiment and Measurement

Intensive shock waves during the process make contactless measurement techniques more dependable and adequate. The laser doppler vibrometer (LDV) combined with an oscilloscope displays the real-time dynamic measurement. A reflective film is glued to the measurement surface to enhance the intensity of the reflected laser beam. The laser head is aligned perpendicularly to the surface of measurement. Each point is measured separately during the process, as only single point laser head was available during the measurement. All measurements are carried out using LDV. The data are then retrieved for post-processing. An illustration of the measuring points is added to the Figure 3.

Modal analysis is a powerful tool for investigating the dynamic properties of a system, in which points of interest are excited via an input force and the response is measured. The process dynamics are measured during the functioning of hammer for supplied pressure of 5 bar and the chisel is initially positioned at 85 mm above the casting. The measured signals are then post-processed in the time domain and in the frequency domain using the fast Fourier transform technique.

2.4. FEM Simulation

The geometry of the machine structure is discretized using finite solid elements. The hammer housing is modeled as a point mass of 27 kg at its center of mass and linked to the structure using the rigid body elements, as shown in Figure 4. The bolt connections are simplified to be bonded joints. The isolator components for machine instalment are modeled using spring and damper elements. The material parameters are tabled in Table 1.

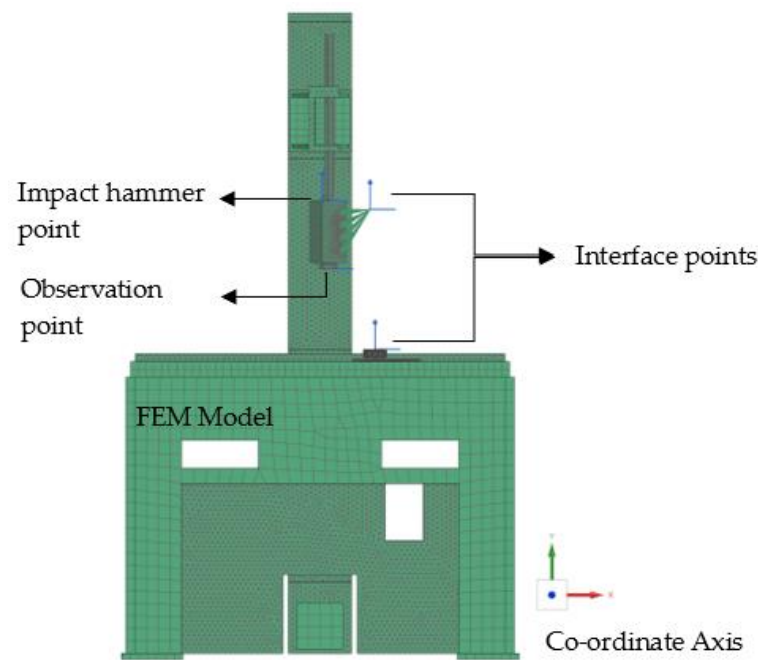


Figure 4. Machine structure FEM.

Table 1. Material parameters—FEM.

Parameter	Material	Density (kg/m^{-3})	Young's Modulus (MPa)	Poisson's Ratio
Structure	Steel	7829	206,940	0.288
Damper	Polyurethane	1230	22	0.45

Newton's equation of motion (EOM) for a system in the time domain can be written as

$$M\ddot{u}(t) + D\dot{u}(t) + Ku(t) = F(t), \quad (1)$$

where $M, C, K \in \mathbb{R}^{f \times f}$ are the global mass and damping and stiffness matrices, respectively. $F(t)$ and $u(t) \in \mathbb{R}^f$ are the time-dependent load and the displacement vector, respectively.

Component mode synthesis (CMS) efficiently describes the system dynamics using fewer DOF by dividing the structural assembly into substructures [20]. A fixed interface mode reduction technique is sought in order to solve the machine structure [17]. Accounting for correct local stiffness with respect to the static stiffness at the interface is important [21].

An illustration of sub-structuring is depicted in Figure 5, in which the larger system is divided into its components A and B. The flexible body A is connected to the rigid body B through the interface node. The component A is modeled using the finite element method, and the connection between the component A and its adjacent component B is defined by interface nodes. Interface degrees of freedom (DOF) are included in the b-set and the interior DOF of component A are defined in the o-set. The partitioning of Equation (1) into b-set and o-set takes the following form:

$$\begin{bmatrix} M_{oo} & M_{ob} \\ M_{bo} & M_{bb} \end{bmatrix} \begin{bmatrix} \ddot{u}_o \\ \ddot{u}_b \end{bmatrix} + \begin{bmatrix} D_{oo} & D_{ob} \\ D_{bo} & D_{bb} \end{bmatrix} \begin{bmatrix} \dot{u}_o \\ \dot{u}_b \end{bmatrix} + \begin{bmatrix} K_{oo} & K_{ob} \\ K_{bo} & K_{bb} \end{bmatrix} \begin{bmatrix} u_o \\ u_b \end{bmatrix} = F(t), \tag{2}$$

and the constrained normal modes are given by solving the following equation:

$$M_{oo} \Psi_{oq} \Omega_{qq} = K_{oo} \Psi_{oq},$$

where the subscript q is the number of fixed interface normal modes, and the constraint modes G_{ob} can be found using

$$G_{ob} = -K_{oo}^{-1} K_{ob}$$

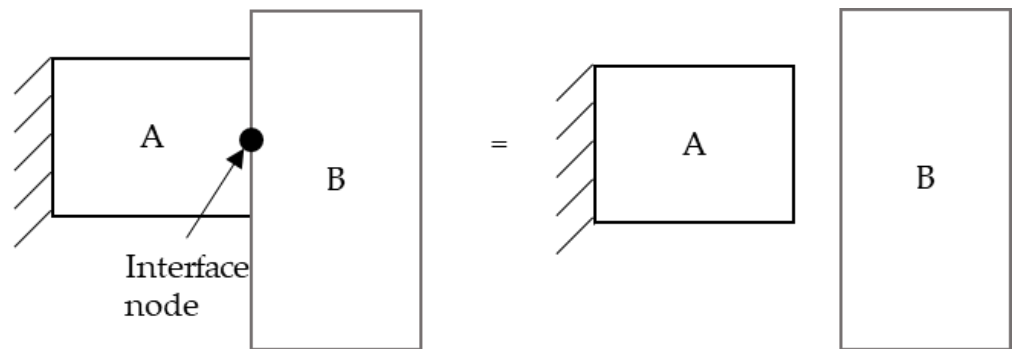


Figure 5. Sub-structuring.

The system response $u(t)$ is given by a combination of the physical response u_b and the generalized response η_q :

$$u(t) = \begin{bmatrix} u_o \\ u_b \end{bmatrix} = \begin{bmatrix} \Psi_{oq} & G_{ob} \\ 0_{bq} & I_{bb} \end{bmatrix} \begin{bmatrix} \eta_q \\ u_b \end{bmatrix} = T_{fz} u_z \tag{3}$$

The reduced form of Equation (1) is obtained by pre-multiplying this equation by T_{fz}^T and substituting Equation (3):

$$M_{zz} \ddot{u}_z + D_{zz} \dot{u}_z + K_{zz} u_z = T_{fz}^T F_f, \tag{4}$$

The natural frequencies Ω_{ss} and the modal vectors Φ_{zs} of the reduced system are then found using the eigenvalue problem:

$$M_{zz} \Phi_{zs} \Omega_{ss} = K_{zz} \Phi_{zs},$$

and the physical response u_z is related to modal response x_s via

$$u_z = \Phi_{zs}x_s, \tag{5}$$

Equation (4) is transformed from the physical domain to the modal domain by substituting Equation (5) and pre-multiplying Φ_{zs}^T as follows:

$$m_{ss}\ddot{x}_s + d_{ss}\dot{x}_s + k_{ss}x_s = \Phi_{zs}^T T_{fz}^T R_{if}^T F_i, \tag{6}$$

the reduced modal mass matrix is obtained via $m_{ss} = \Phi_{zs}^T M_{zz} \Phi_{zs}$, and the same conversion applies to stiffness and damping matrices. The state space form of Equation (6) is then

$$\begin{bmatrix} \dot{x}_s \\ \ddot{x}_s \end{bmatrix} = \begin{bmatrix} 0_{ss} & I_{ss} \\ -m_{ss}^{-1}k_{ss} & -m_{ss}^{-1}d_{ss} \end{bmatrix} \begin{bmatrix} x_s \\ \dot{x}_s \end{bmatrix} + \begin{bmatrix} 0_{si} \\ m_{ss}^{-1}\Phi_{zs}^T T_{fz}^T R_{if}^T \end{bmatrix} F_i \text{ and}$$

$$\begin{bmatrix} y_j \\ \dot{y}_j \\ \ddot{y}_j \end{bmatrix} = \begin{bmatrix} S_{jf}T_{fz}\Phi_{zs} & 0_{js} \\ 0_{js} & S_{jf}T_{fz}\Phi_{zs} \\ -S_{jf}T_{fz}\Phi_{zs}m_{ss}^{-1}k_{ss} & -S_{jf}T_{fz}\Phi_{zs}m_{ss}^{-1}d_{ss} \end{bmatrix} \begin{bmatrix} x_s \\ \dot{x}_s \end{bmatrix} + \begin{bmatrix} 0_{js} \\ 0_{js} \\ S_{jf}T_{fz}\Phi_{zs}m_{ss}^{-1}\Phi_{zs}^T T_{fz}^T R_{if}^T \end{bmatrix} F_i,$$

The full model of the output (DOF) of the f-set is reduced to collect only a subset DOF of interest. The matrix R_{jf} and S_{jf} are partition matrices to reduce the full set-f to subsets i and j for input and output vectors, respectively.

The simplified form of the above equation is written as below, where superscript (m) denotes that the vector or matrix belong to the machine structure.

$$\dot{X}_{2s}^m = A^m X_{2s}^m + B^m F_i^m, \tag{7}$$

$$Y_{3j}^m = C^m X_{2s}^m + D^m F_i^m, \tag{8}$$

The nodes connecting the hammer and casting to machine mark the interface nodes. The state vectors describing the nodes are considered only in the vertical direction corresponding to the excitation direction. The system is modeled and solved using NX Nastran code in Simcenter 3D from Siemens PLM Software Inc., 2021.1, Plano, TX, USA.

The performed modal analysis provides the response of the system for the undamped system, while in practice, the system is damped. A modal damping approach is adopted to coarsely capture the system’s damping behavior. The damping matrix is modeled as $d = 2\xi \cdot m_{ss} \cdot \text{diagonal}(\Omega_1, \dots, \Omega_s)$, where ξ is the damping ratio adapted to the experimental modal analysis.

2.5. Multibody Modeling

A de-coring hammer is fundamentally a pneumatic hammer delivering impulse force to the casting. The hammer studied here has tandem operations, as mentioned in Section 3. A simplified line body diagram for the hammer and casting is depicted in Figure 6. The dynamics of the system are specified using Newton’s second law of motion, as mentioned in Equation (1). The supplied air pressure drives the de-coring hammer. Impact force, due to contact between the components, is modeled using a non-linear spring and damper system. The impact force between piston, chisel, and casting is particularly significant to determine the characteristics of the process.

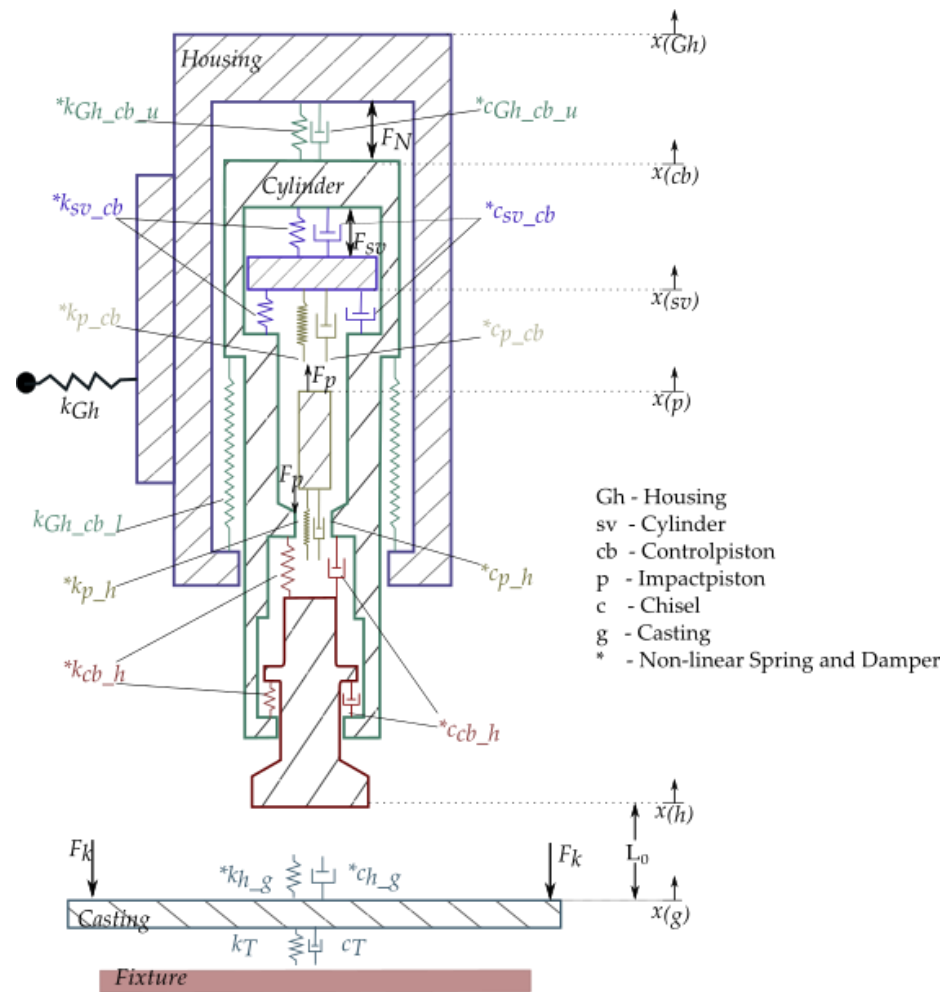


Figure 6. Lumped-mass model.

The stiffness of each component is obtained using the inertia relief technique in FEM and the impact stiffness (k_c) and damping (d_c) are described using the model proposed in [16]. The force (F) vector is obtained through Equation (9), and the friction force (F^f) is described as viscous damping in Equation (10):

$$F = PA + F^f, \tag{9}$$

$$F^f = -f^v \dot{x}(t) \tag{10}$$

Special attention for friction on the cylinder is given to model the non-linear friction effects on the cylinder. The cylinder is mounted with a plastic element on the top to induce a stick and slip friction and direction specific damping. The friction is modeled as a combination of static and viscous friction to accommodate the stick and slip course and a Heaviside function (H) to account for the direction of force.

$$F^{c-f} = -f^s + f^f + f^d H, \tag{11}$$

$$H = \begin{cases} u^1 & \text{if } \dot{x}(t) \leq 0 \\ u^2 & \text{if } \dot{x}(t) > 0 \end{cases} \tag{12}$$

The dynamic state variables for the MBS model in its generalised form are

$$\dot{X}_{2v}^h = A_{2v \times 2v}^h X_{2v}^h + B_{2v \times v}^h F_v^m, \tag{13}$$

$$Y_{2v}^h = C_{2v \times 2v}^h X_{2v}^h + 0 \tag{14}$$

Regarding the transformation matrices, C^h is an identity square matrix and B^h is a boolean matrix. The outputs are not influenced by input, and therefore, the E matrix is zero. The pressure derivatives are detailed in the work of Richer [14] and are denoted by

$$\dot{P} = \frac{RT}{V_0} (\alpha_{in} \dot{m}_{in} - \alpha_{out} \dot{m}_{out}) + \frac{\alpha P A \dot{x}(t)}{(V_0 \pm A x(t))} \tag{15}$$

The pneumatic and dynamic systems are coupled and solved using MATLAB R2022a, The MathWorks Inc., Albuquerque, NM, USA. The formulation of the MBS model is charted in Figure 7. Furthermore, the mechanical properties of the components are given in Table 2.

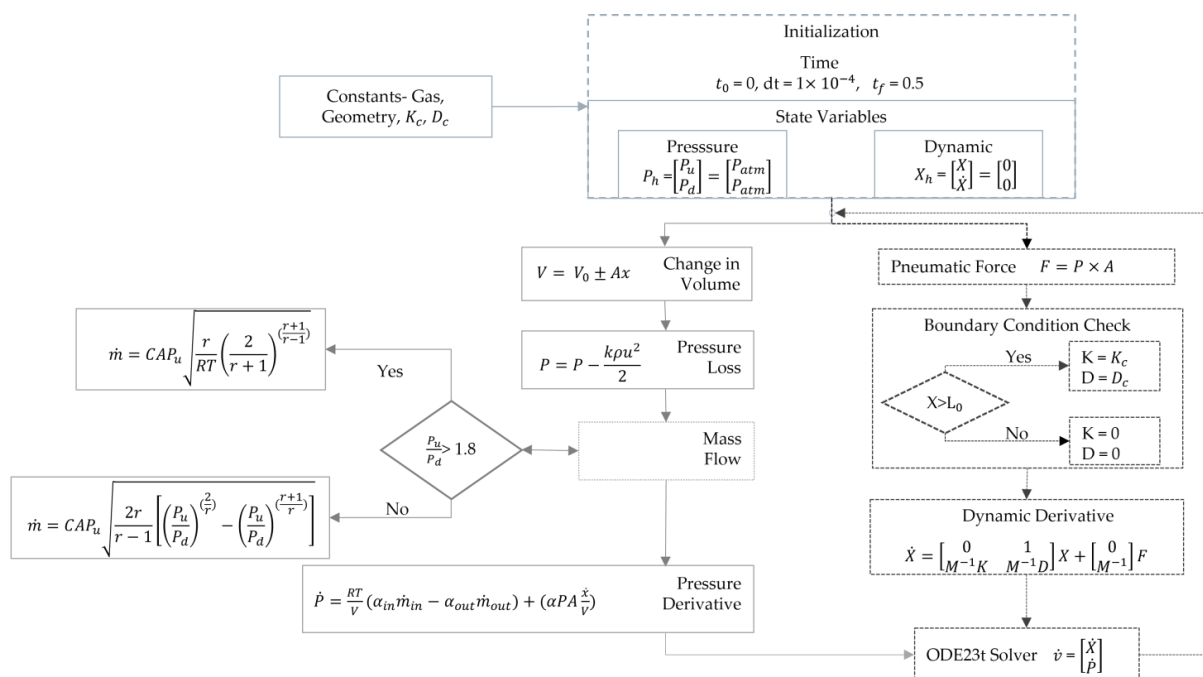


Figure 7. MBS model flowchart.

Table 2. MBS model parameters.

Mass (Kg)		Stiffness (N/m)		Damping (Ns/m)	
m_{Gh}	1	k_{Gh}	1×10^{10}	$c_{Gh_cb_u}$	1.633
m_{cb}	6.5	$k_{Gh_cb_u}$	1.633×10^4	$c_{Gh_cb_l}$	0.1633
m_{sv}	74×10^{-3}	$k_{Gh_cb_l}$	1.633×10^3	c_{sv_cb}	1650
m_p	0.4546	k_{sv_cb}	1.0121×10^7	c_{p_cb}	2000
m_h	1.8157	k_{p_cb}	2×10^7	c_{p_h}	1500
m_g	0.517	k_{p_h}	5.971×10^8	c_{cb_h}	1052
		k_{cb_h}	6.06×10^8	c_T	4000
		k_T	3×10^7	c_{h_g}	500
		k_{h_g}	2.95×10^8		

There are a total of twelve dynamic and four pressure state variables defining the hammer model. The MATLAB Solver ode23t [22] was selected due to its stiff equation caused by impacts. The impact is identified based on the detection of contact, as defined by the boundary and position. A non-linear spring and damper are activated upon detecting contacts, with collision stiffness and damping between each component.

2.6. Coupled Simulation

The hammer is mounted statically to the machine structure, and the casting is mounted to the fixture on the machine table. Figure 8 depicts the coupling of the FEM and MBS model. The connection between the hammer housing and machine is established through a linear spring (k_{Gh}) of high stiffness. The casting and the fixture connection is modeled as a linear spring-damper system (k_T, c_T).

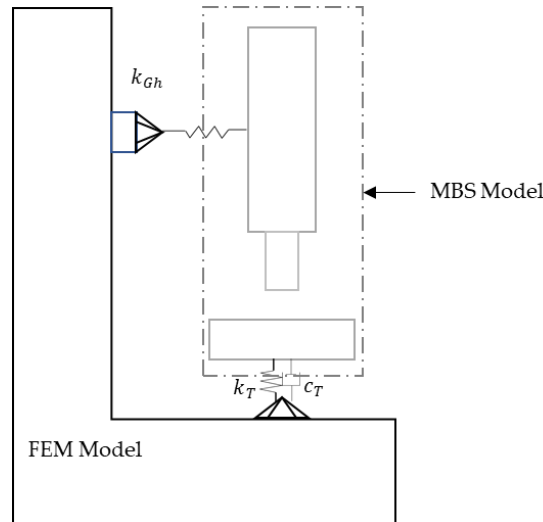


Figure 8. Flexible body coupling.

The static connection to the system is added to the state space matrix as follows: the force transferred between the MBS and FEM model through the springs and damper.

$$f_{node1} = k_{Gh}[-x_{node1} + x_{Gh}] \text{ and } f_{node2} = k_T[-x_{node2} + x_g] + d_T[-\dot{x}_{node2} + \dot{x}_g]$$

Rewriting the above equation using state variables and a transformation using C matrix yields, we obtain:

$$f_{node1} = -f_{Gh} = k_{Gh}[-C1^{n1} \quad C2^{gh}] \begin{bmatrix} X^m \\ X^h \end{bmatrix} \text{ and} \tag{16}$$

$$f_{node2} = -f_T = [k_T \quad d_T] \begin{bmatrix} -C1^{n2} & C2^g \\ -C1^{\bar{n}2} & C2^{\bar{g}} \end{bmatrix} \begin{bmatrix} X^m \\ X^h \end{bmatrix} \tag{17}$$

And the row vector $C1 \subseteq C_{3j \times 2s}^m$ is obtained through the following notions:

$$C1_{1 \times 2s}^{n1} = [C_{(n1,1)}^m, C_{(n1,2)}^m, \dots, C_{(n1,2s)}^m],$$

$$C1_{1 \times 2s}^{n2} = [C_{(n2,1)}^m, C_{(n2,2)}^m, \dots, C_{(n2,2s)}^m], \text{ and } C1_{1 \times 2s}^{\bar{n}2} = [C_{(j+n2,1)}^m, C_{(j+n2,2)}^m, \dots, C_{(j+n2,2s)}^m]$$

The row vector $C2 \subseteq C_{2v \times 2v}^h$ is similarly derived. The subscripts $n1, n2$ and $g1, g2$ define the row index of the components for coupling nodes in FEM and corresponding bodies in MBS, respectively. Performing transformation on the newly derived coupling force vector obtained in Equations (16) and (17) with matrix B^m from Equation (7) and moving the state variables out yields the following form:

$$B^m \begin{bmatrix} f_{node1} \\ f_{node2} \end{bmatrix} = \begin{bmatrix} B^m \begin{bmatrix} -k_{Gh}C1^{n1} \\ -k_T C1^{n2} - d_T C1^{\bar{n}2} \end{bmatrix} & B^m \begin{bmatrix} k_{Gh}C2^{gh} \\ k_T C2^g + d_T C2^{\bar{g}} \end{bmatrix} \end{bmatrix} \begin{bmatrix} X^m \\ X^h \end{bmatrix} \tag{18}$$

Similar transformations for f_{Gh} and f_T can be shown by considering Equations (13), (16) and (17). Now, including the newly arrived form of the transformed coupling force vectors and combining Equations (7) and (13) yields the following equation:

$$\begin{bmatrix} \dot{X}^m \\ \dot{X}^h \end{bmatrix} = \begin{bmatrix} A^m + B^m \begin{bmatrix} -k_{Gh}C1^{n1} \\ -k_T C1^{n2} - d_T C1^{n2} \end{bmatrix} & B^m \begin{bmatrix} k_{Gh}C2^{Gh} \\ k_T C2^g + d_T C2^g \end{bmatrix} \\ B^h \begin{bmatrix} k_{Gh}C1^{n1} \\ 0_{h-2 \times 2v} \\ k_T C1^{n2} + d_T C1^{n2} \end{bmatrix} & A^h + B^h \begin{bmatrix} -k_{Gh}C2^{Gh} \\ 0_{h-2 \times 2v} \\ -k_T C2^g - d_T C2^g \end{bmatrix} \end{bmatrix} \begin{bmatrix} X^m \\ X^h \end{bmatrix} + \begin{bmatrix} B^m & 0_{2s \times h} \\ 0_{2v \times i} & B^h \end{bmatrix} \begin{bmatrix} 0_i \\ F^h \end{bmatrix},$$

There is no internal force acting on the hammer station and the coupling force is added to the A matrix; therefore, the force vector for the machine is zero. The force vector F^h defines the internal force acting on the hammer due to pneumatic pressure. The pressure state variables remain unaffected by this transformation.

3. Measurement Results

The de-coring machine equipped with LDV considered in this study is shown in Figure 9. The labelled sections are the hammer (1), machine structure (2), laser head (3), signal processor (4), casting (5), fixture (6), and laser point (7). The hammer is supplied with pressurised air at 5 bar, and the casting is placed at 85 mm below the chisel. The vibrational velocity at the measurement points is collected using the LDV, as described in the Materials and Methods section. The sensitivity of the laser vibrometer needs to be adjusted to correspond to the magnitude of vibration. The measured signals are exported to MATLAB for post-processing.

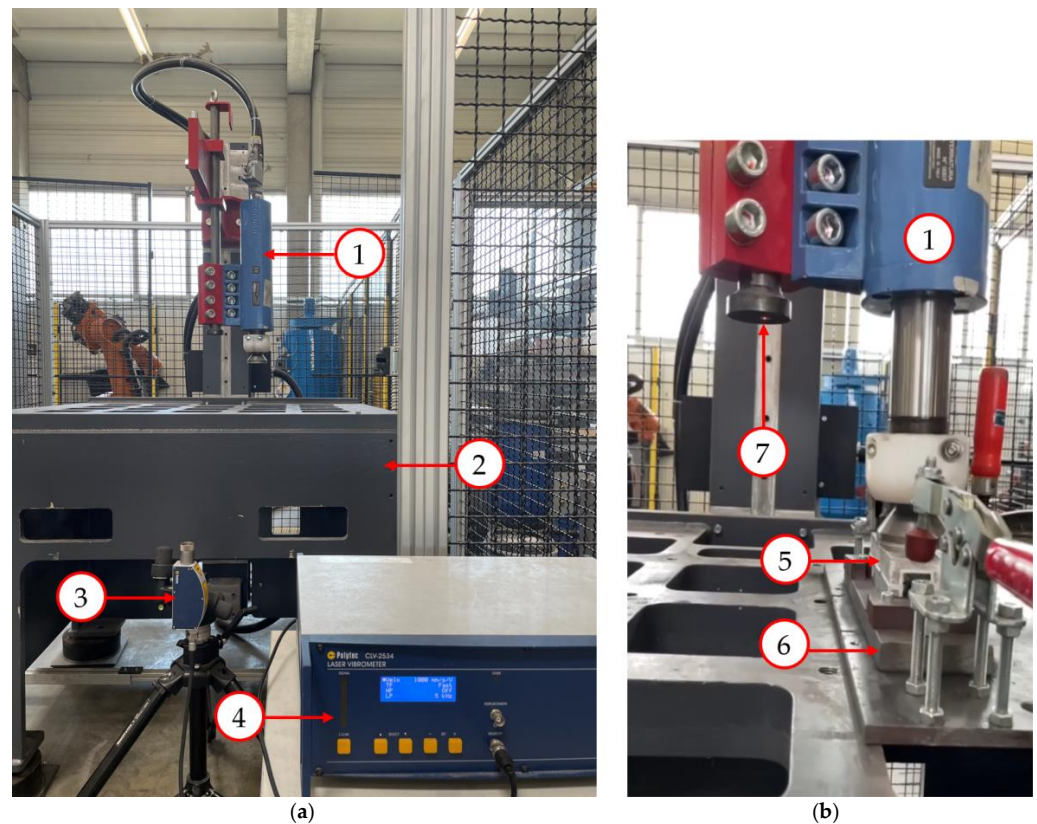


Figure 9. (a) De-coring machine with single hammer and measuring unit, and (b) measuring hammer arm vibration.

LDV sensitivity is set at 10 mm/s/V for measuring the hammer arm vibration and at 1000 mm/s/V to read the chisel vibration, as plotted in Figure 10. The quality of the measured signal is degraded due to the speckle effect, a common measurement error using an LDV, which causes signal dropouts [23]. The loss of the reflected waves causes sharp peaks in the measurement, seen in the chisel measurement as single sharp peaks.

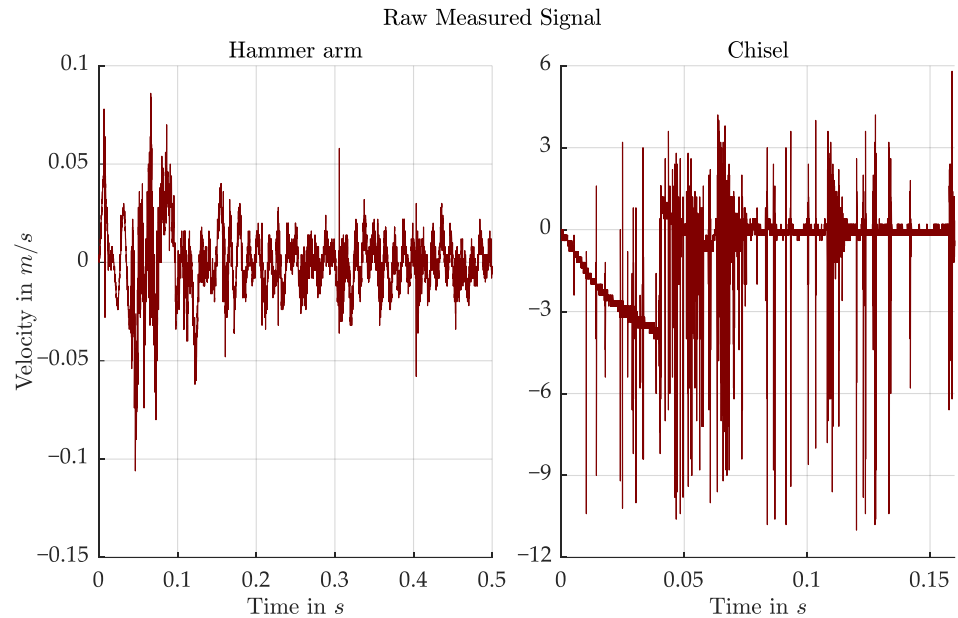


Figure 10. Velocity measurement of hammer arm at 10 mm/s/V and chisel at 1000 mm/s/V.

Vibrations in casting are measured at three different sensitivities of LDV, as seen in Figure 11. Low magnitude vibrations are better measured at 10 mm/s/V sensitivity of LDV, which are modulated by noises at 1000 mm/s/V sensitivity. Signal dropouts can also be seen in the casting vibration measurements. All measurement signals are post-processed to improve signal quality.

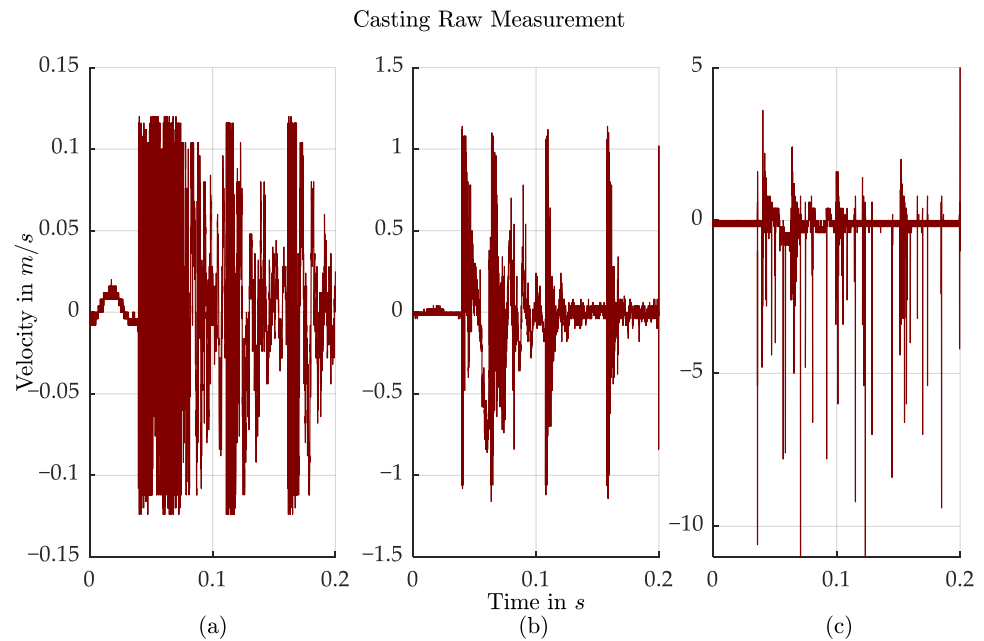


Figure 11. Casting velocity measurement at sensitivities (a) 10 mm/s/V, (b) 100 mm/s/V and (c) 1000 mm/s/V.

The measured time signals are treated with a Butterworth low pass filter to remove artifacts from measurement. The filtered signals for hammer arm and chisel are plotted in Figure 12. The resolution of the signal is improved through low pass filter with a cut off frequency at 4000 Hz, and signal dropouts are isolated for easier identification. Post-treated casting measurement with a low pass filter for selected sensitivities are plotted in Figure 13. Velocity peaks during impacts are identifiable in the signal measured at a 1000 mm/s/V sensitivity.

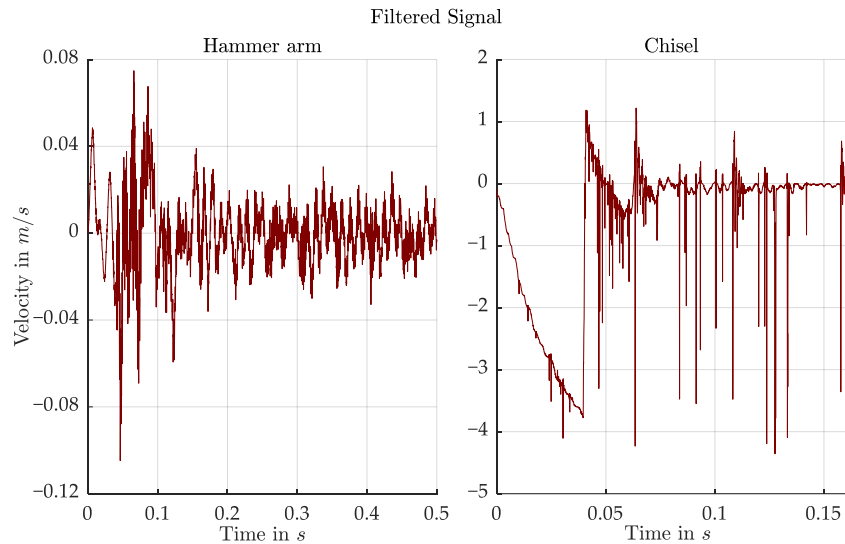


Figure 12. Filtered measurement signal of hammer arm and chisel velocity.

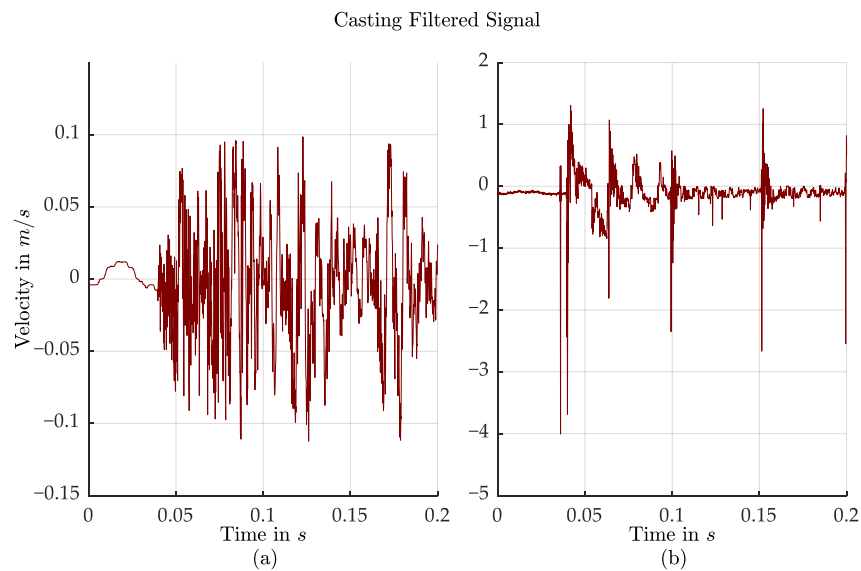


Figure 13. Filtered measurement signals of casting velocity (a) 10 mm/s/V and (b) 1000 mm/s/V.

Upon supplying air pressure, the chisel and cylinder arrangement accelerate towards casting. An oscillatory response in the casting and hammer arm is recorded during the cylinder extension phase before the chisel contacts the casting. The impact between the chisel and casting causes the chisel to rebound and the casting to also move upwards. The shock is transferred to the hammer arm. The chisel is forced onto casting and delivers periodic hits on the casting with a lower rebound velocity. The rebound velocity shows the difference in delivered energy between the first impact and subsequent periodic impacts. The periodical impacts are due to the piston force. The recorded casting velocity differs in the frequency of impact for measurements at different sensitivities. In particular, the

frequency of third impact measured at a sensitivity of 1000 mm/s/V is higher compared to other signals shown in Figure 11. The response of the chisel and hammer arm could not be measured due to a lack of synchronization during measurement.

4. Simulation Results and Discussion

In this section, the FEM model is validated and the coupled simulation results are compared against the measurements. The FEM model of the structure is simplified and reduced using the fixed interface method. The global damping parameters are estimated using the modal analysis and the damping matrix is defined. The reduced model of the structure is integrated to the MBS model and a coupled flexible rigid simulation is executed. Coupled simulation results are then compared against the measurements.

4.1. FEM Model Validation

Machine structure is discretised using finite elements and the point of interface is defined using fixed interface joints. The interface nodes are connected to the machine structure using the rigid body elements. The simplified model and the structural elements are glued down to restrict sliding. The mass of the hammer housing is added to the interface node 1.

The comparison of the measured and calculated natural frequency is shown in Table 3. Natural frequencies found under 10 Hz belong to damping elements isolating the machine from the ground. Natural frequencies at 25, 32, and 54 Hz are not found in the calculated model.

Table 3. Comparison of system natural frequency.

Measured (Hz)	Calculated (Hz)	Difference (%)
16	16.29	−1.81%
18	18.61	−3.39%
21	19.93	5.10%
44	44.69	−1.57%
79	81.55	−3.23%
85	84.81	0.22%
90	91.53	−1.70%
118	117.35	0.55%
148	144	2.70%
208	212	−1.92%
231	231.85	−0.37%
271	278.61	−2.81%

The machine structure is excited with an input force and the vibration velocity is measured as the response. The input and output nodes are matched for experimentation, and a global damping of 2% is specified in the simulation. The dynamic mobility measured is plotted against the simulation in Figure 14.

The global damping factor captures the trend of the natural frequency with little deviation. Model simplification has shifted the natural frequencies of the FEM model. The frequency at 32 Hz in the simulation is underrepresented. The linearised model captures the system characteristics well. The model is then reduced as described in Section 2.4. FEM Simulation, and the results of dynamic simulation are discussed further in the following section.

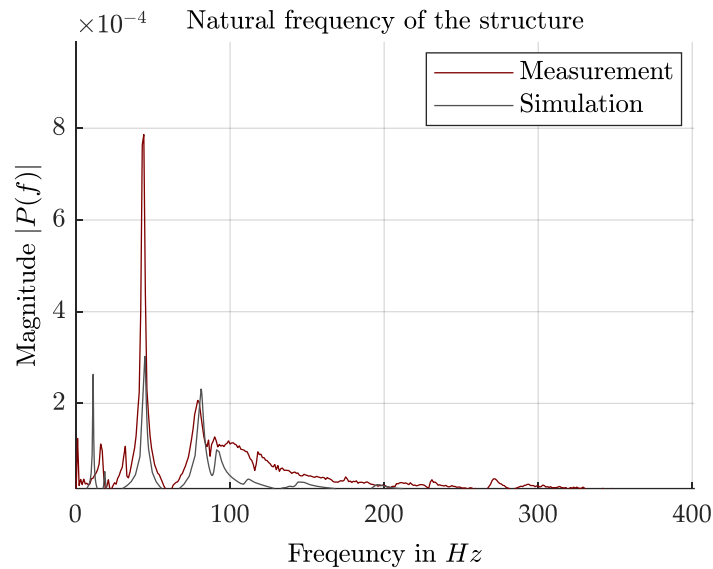


Figure 14. Natural frequency of the machine structure.

4.2. Process Simulation

The reduced-order model is then coupled with the non-linear de-coring hammer model. The system is initialised under the same conditions as the measurements. The supplied air pressure is assumed to reach the hammer at 5 bar and be free of fluctuations. The simulation is carried at time steps of 1×10^{-5} s. The results obtained from the simulation are compared and discussed in this section.

The hammer arm oscillation velocity measured and simulated for the process conditions are compared in Figure 15. The initial oscillation in the hammer arm during the cylinder extension phase in the simulation agrees with the measurements. Shock generated in the hammer arm is distinguished from the impact of chisel on the casting at the end of the extension. During the hammering phase, the magnitude of oscillation is higher for the simulated model compared to the measurements. The oscillation tends to decrease in magnitude over time.

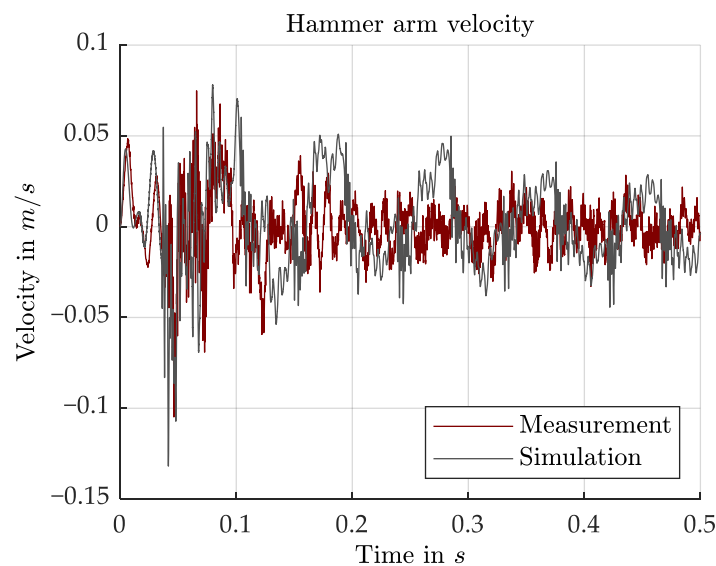


Figure 15. Hammer arm velocity measurement and simulation comparison.

The acceleration of the chisel during extension as well as its rebound velocity after the first impact is faster in the calculated model (in Figure 16). The frequency of impact

is not constant for measurement and simulation. The periodic impacts between casting and chisel have a frequency of around 22 Hz for the calculated model and around 20.5 Hz for the measurements. The impact velocity of the chisel has a similar magnitude to the measurement.

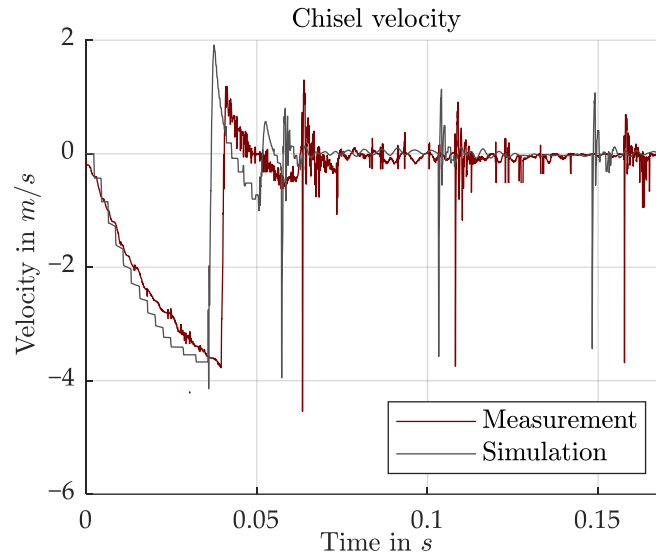


Figure 16. Chisel velocity measurement and simulation comparison.

The initial impact peak of casting is well captured in the simulation, as plotted in Figure 17. Subsequent impact peaks vary between simulation and measurement. The second impact peak in simulation has a difference of 3.85 in magnitude to the measured velocity. It should be noted that casting velocity is measured from the bottom and not at the point of impact. The lateral deformation of casting and the measurement point is suspected to cause this difference. An attempt to verify this is not possible due to the restriction of measurement possibilities.

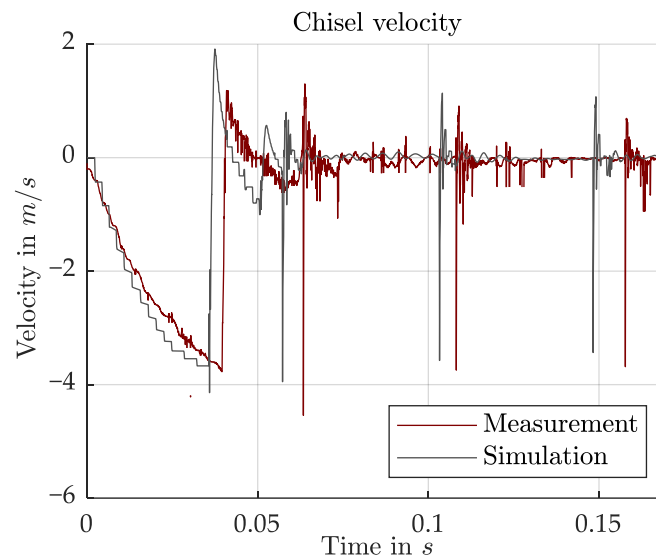


Figure 17. Casting velocity measurement and simulation comparison.

The frequencies of the signal are calculated using fast Fourier transform (FFT) to further evaluate the process. The signal is divided in order to study each stage separately. The hammer arm signal is separated for the extension phase and the other impacts during hammering phase. Separated signals are then transformed via FFT. The measured

and simulated signals are treated in the same manner and compared in Figure 18. The time domain signal is plotted at the top, and its corresponding FFT of up to 1000 Hz is plotted below.

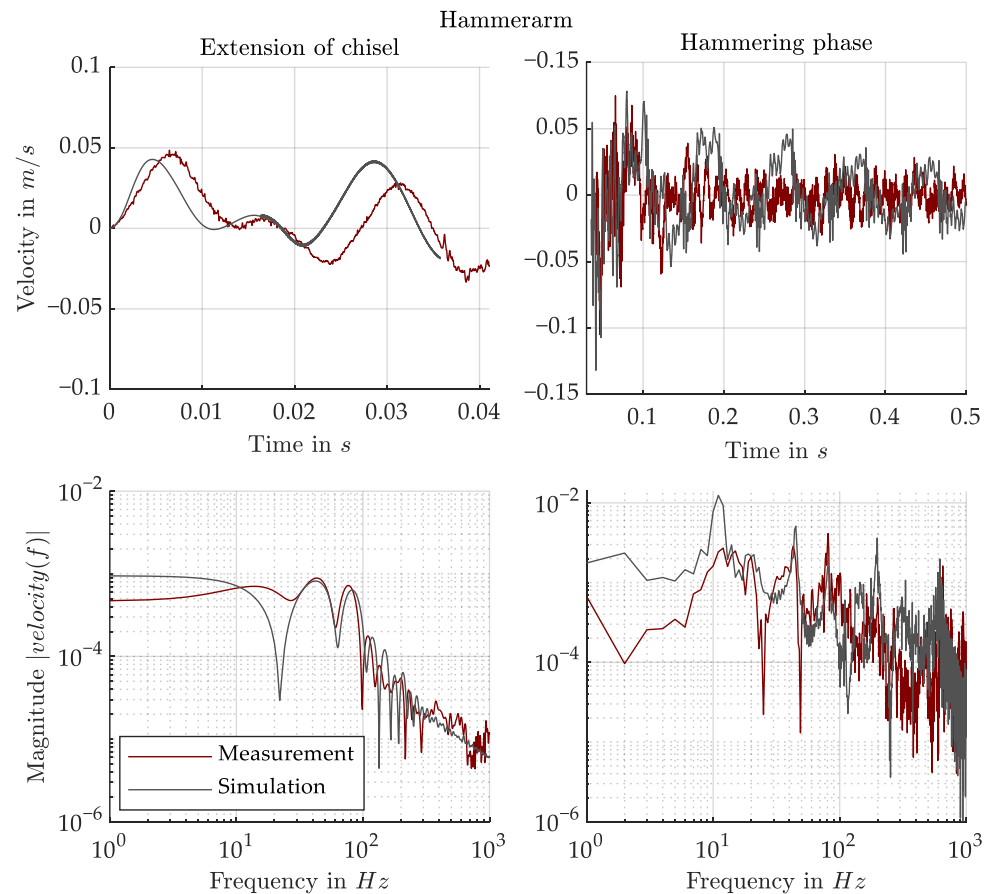


Figure 18. Hammer arm FFT comparison.

The hammer arm swings at its natural frequency upon supplying air pressure. The frequency shift due to model simplification dampens the oscillation at 21 Hz in the simulation. Additionally, a change in system stiffness is measured during the extension phase. The root mean square (RMS) values of the measured and simulated signals during this phase are 0.0209 and 0.0216, respectively. During the hammering phase, where the piston exerts impact force on chisel, the first impact from the chisel is studied via its frequency. The system excitation at its natural frequencies is recorded with similar intensity for measured and simulated values, except for the shifted frequency below 15 Hz. Contrary to expectation, the hammer arm excitation at hammering frequency is underrepresented in both the simulations and measurements. Oscillation at 44 Hz dominates the simulated system and 81 Hz has dominance in the measured signal. Although global damping applied to the machine structure captures the trends of a physical system, it underestimates the frequency-based damping of the system. The vibration signal has RMS values of 0.0137 and 0.0254 for measurements and simulations.

The chisel velocity is studied via two impacts to characterise its behavior during de-coring. Chisel velocity is isolated until first contact with the casting and rebound; then FFT is carried out. Single periodic impacts for measurement and simulation are compared. The time signals and their FFT are plotted and are shown in Figure 19. The time for the single periodic impact measurement is not exact, but overlaid on the simulation signal to show the duration of impact.

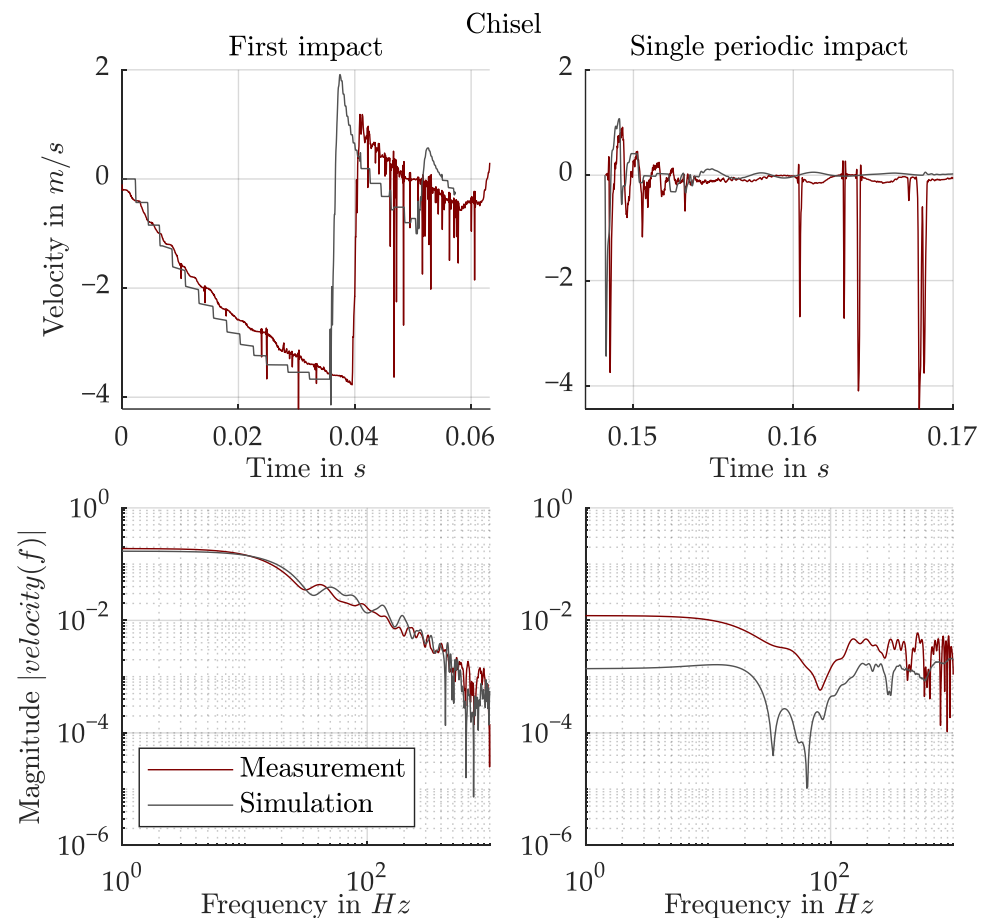


Figure 19. Chisel FFT comparison.

Staircase profile in chisel velocity is caused due to bushing the component between the cylinder and chisel, and the profile is distorted in the raw measured signal. The rebound velocity of the hammer is suppressed in the measurement. The effect is assumed to be caused by the non-linear characteristics of bushing on the cylinder. Higher rebound velocity in simulation causes the chisel to re-excite. The signal dropouts in the measurement during periodic impacts manipulates the intensity of the FFT plot. The time domain comparison illustrates that the modeled impact follows the measurement trend.

A similar comparison is presented for casting in Figure 20. The rebound velocity of the casting is larger in simulation compared to measurement. The excitation of table due to initial chisel displacement is minimal and has very little influence on casting. Contact properties between fixture and casting is another vital aspect for de-coring.

The excitation of hammer arm at 81 Hz induces a rotational vibration to hammer, and the tilting of the hammer causes contact misalignment between the chisel and casting. This contact misalignment impedes the laser reflection, causing signal dropouts in the measurements.

The presented model agrees with the dynamic characteristics of the system and represents the non-linear effects during the process to a considerable level. The process characteristic is studied as a one-dimensional problem, restricting the focus to major force vectors.

The energy delivered by the hammer is distinct during the first impact relative to the continued impacts by the inner moving piston. The parameter is quantified through the simulation and validated through experiments. Excitation on the casting in the first stage is vital to break the sand core. Although the continued impacts by the piston bring additional energy to core vibration, its role is yet to be distinguished. The model developed in this work has encouraged the identification of critical parameters that interact during

the interactions of the casting and the hammer. The parameters will be further investigated to qualify their consequences in the process.

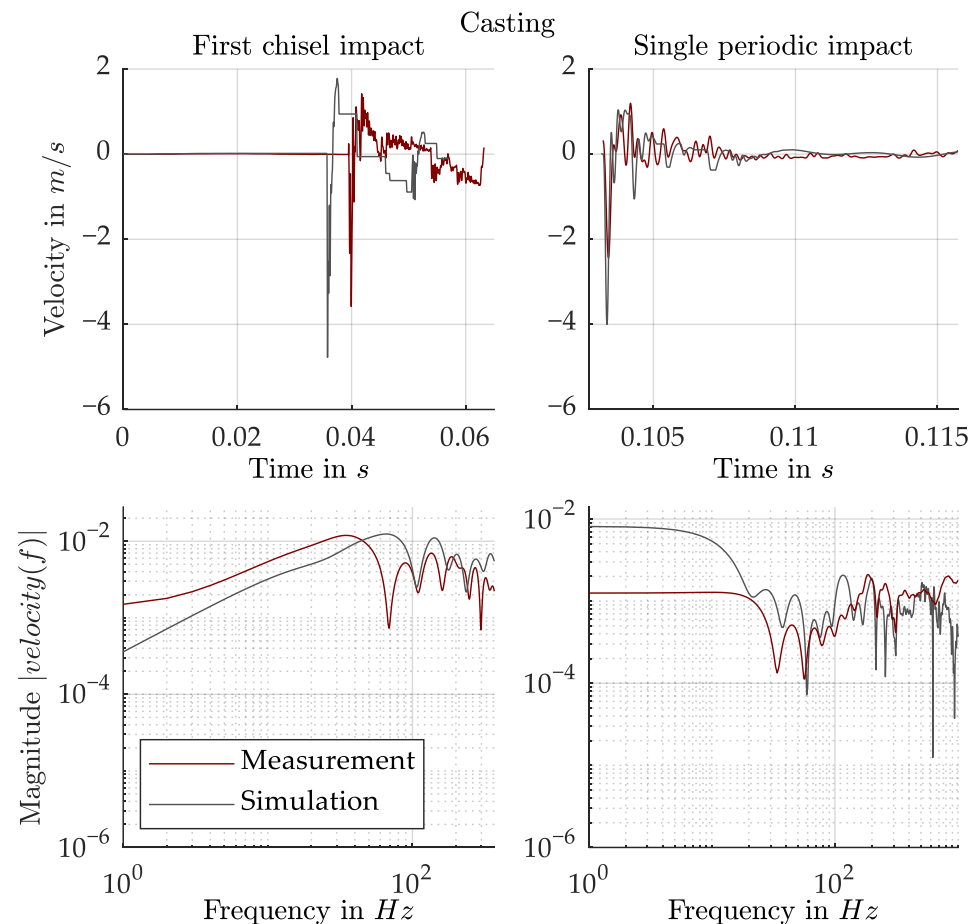


Figure 20. Casting FFT comparison.

5. Conclusions

An industrial-based de-coring process was simulated and experimentally validated. Casting subjected to de-coring was approached in two stages in the process. This work demonstrates a method to determine the forces and the dynamic characteristics of the process. The average difference between the calculated model and measurement for impact velocity of chisel is -6.56% and for that of casting is 48.32% . A possible cause for this difference was discussed in a previous section. The frequency of the chisel impact is 6.5% higher than in the calculated model. The RMS value of simulated signal and measured signal has a higher deviation of 85% during the hammering phase. The de-coring hammer delivers 70 J at the first impact from the rest position and 12.2 J on average during the hammering phase for the assumed operating conditions.

The mathematical formulation presented in this study facilitates the digitalization of the process and aids in the investigation of the process parameters. The main conclusion of this work is summarized as follows:

1. The impact force delivered to the casting varies significantly between the first impact and subsequent impacts.
2. The impact force and dynamic characteristics during the de-coring process can be predicted using the presented model. The model results can be applied to perform de-coring simulation or prevent damage to the casting part.
3. This method can be used to investigate the effect of clamping forces and fixture materials.
4. The working frequency of the hammer depends on the dynamic characteristics of the system.

5. The developed model will be implemented in industrial cast parts in the future.

The influence of the chisel geometry is another interesting quantifier that will be explored in the future work. The characteristics of the de-coring tool were quantified in this study. The approach presented in this work shows good agreement with the measurements, considering the non-linearity of the system. The model can be further improved through the frequency-based damping of the system. This method can be extended to more than one dimension using the theory presented in this paper.

Author Contributions: Conceptualization, M.M., D.G. and W.V.; methodology, M.M. and R.B.; formal analysis, M.M.; Validation, M.M., D.G. and R.B.; resources, F.E. and D.G.; data curation, M.M.; writing—original draft preparation, M.M.; writing—review and editing, M.M. and D.G.; visualization, M.M.; supervision, W.V. All authors have read and agreed to the published version of the manuscript.

Funding: The APC was funded by the Fill Gesellschaft, m.b.H.

Data Availability Statement: The data supporting this study's findings are available from the corresponding author upon reasonable request. The data are not publicly available due to the privacy restrictions of the machine manufacturer.

Acknowledgments: The author gratefully acknowledges the support of Fraunhofer IGCV in facilitating the experimental work. Gratitude and thanks to my colleagues in Fill GmbH, especially Harald Sehrschön for his immense support, Thomas Murauer for sharing his expertise and guidance, and Gerhard Sieglhuber for his support in the experimental setup.

Conflicts of Interest: Authors Melvin Mariadass and Roman Binder were employed by the company Fill Gesellschaft, m.b.H., Gurten, Austria. The APC was funded by the Fill Gesellschaft m.b.H. The funder was not involved in the study design, collection, analysis, interpretation of data, the writing of this article, or the decision to submit it for publication.

References

1. Izdebska-Szanda, I.; Angrecki, M.; Matuszewski, S. Investigating of the Knocking Out Properties of Moulding Sands with New Inorganic Binders Used for Castings of Non-ferrous Metal Alloys in Comparison with the Previously Used. *Arch. Foundry Eng.* **2012**, *12*, 117–120.
2. Czerwinski, F.; Mir, M.; Kasprzak, W. Application of cores and binders in metalcasting. *Int. J. Cast Met. Res.* **2015**, *28*, 129–139. [[CrossRef](#)]
3. Stauder, B.J. Investigation on the Removal of Internal Sand Cores from Aluminium Castings. Ph.D. Thesis, Montan Universität, Leoben, Austria, 2018.
4. Stauder, B.J.; Gruber, D.; Schumacher, P. Specific fracture energy and de-agglomeration rate of silicate-bonded foundry sand cores. *Prod. Eng.* **2018**, *12*, 807–816. [[CrossRef](#)]
5. Stauder, B.J.; Harmuth, H.; Schumacher, P. De-agglomeration rate of silicate bonded sand cores during core removal. *J. Mater. Process. Technol.* **2018**, *252*, 652–658. [[CrossRef](#)]
6. Stauder, B.J.; Kerber, H.; Schumacher, P. Foundry sand core property assessment by 3-point bending test evaluation. *J. Mater. Process. Technol.* **2016**, *237*, 188–196. [[CrossRef](#)]
7. Stauder, B.J.; Berbic, M.; Schumacher, P. Mohr-Coulomb failure criterion from unidirectional mechanical testing of sand cores after thermal exposure. *J. Mater. Process. Technol.* **2019**, *274*, 116274. [[CrossRef](#)]
8. Lechner, P.; Fuchs, G.; Hartmann, C.; Steinlehner, F.; Etemeyer, F.; Volk, W. Acoustical and Optical Determination of Mechanical Properties of Inorganically-Bound Foundry Core Materials. *Materials* **2020**, *13*, 2531. [[CrossRef](#)] [[PubMed](#)]
9. Dong, S.; Iwata, Y.; Hohjo, H.; Iwahori, H.; Yamashita, T.; Hirano, H. Shell Mold Cracking and Its Prediction during Casting of AC4C Aluminum Alloy. *Mater. Trans.* **2010**, *51*, 1420–1427. [[CrossRef](#)]
10. Lechner, P.J. A Material Model for Foundry Cores-The Brittle Fracture Behaviour of Chemically-Bound Foundry Sands. Ph.D. Thesis, Technical University of Munich, Munich, Germany, 2021; pp. 71–95. Available online: <https://mediatum.ub.tum.de/?id=1635091> (accessed on 20 November 2023).
11. Etemeyer, F.; Schweinefuß, M.; Lechner, P.; Stahl, J.; Greß, T.; Kaindl, J.; Durach, L.; Volk, W.; Günther, D. Characterisation of the decoring behaviour of inorganically bound cast-in sand cores for light metal casting. *J. Mater. Process. Technol.* **2021**, *296*, 117201. [[CrossRef](#)]
12. Dobmeier, F.; Li, R.; Etemeyer, F.; Mariadass, M.; Lechner, P.; Volk, W.; Günther, D. Predicting and Evaluating Decoring Behavior of Inorganically Bound Sand Cores, Using XGBoost and Artificial Neural Networks. *Appl. Sci.* **2023**, *13*, 7948. [[CrossRef](#)]
13. Richer, E.; Hurmuzlu, Y. A High Performance Pneumatic Force Actuator System Part 1—Nonlinear Mathematical Model. *ASME J. Dyn. Syst. Meas. Control* **2000**, *122*, 416–425. [[CrossRef](#)]

14. Didier, W. Development and Validation of a Mathematical Model for Predicting the Performance of Rotary Hammer Drills. Master's Thesis, University of Wisconsin-Milwaukee, Milwaukee, WI, USA, 2013.
15. Xu, X.; Xu, X.; Liu, W.; Zhou, D. A New Formula of Impact Stiffness in Linear Viscoelastic Model for Pounding Simulation. *Shock Vib.* **2016**, *2016*, 5861739. [[CrossRef](#)]
16. Nakhimovski, I. Modeling and Simulation of Contacting Flexible Bodies in Multibody Systems. Licentiate Thesis, Linköping University, Linköping, Sweden, 2002.
17. Craig, R.R.; Kurdila, A.J. *Fundamentals of Structural Dynamics*; John Wiley & Sons: Hoboken, NJ, USA, 2006.
18. Binder, R.; Wiesauer, M. Analyzing the Impact of Different Drive Concepts on Machine Tool Dynamics Using Mechatronic System Simulation. In Proceedings of the NAFEMS, online, 25–29 October 2021.
19. Scheel, M.; Gibanica, M.; Nord, A. State-Space Dynamic Substructuring with the Transmission Simulator Method. *Exp. Tech.* **2019**, *43*, 325–340. [[CrossRef](#)]
20. Craig, R.R.; Bampton, M.C.C. Coupling of substructures for dynamic analyses. *AIAA J.* **1968**, *6*, 1313–1319. [[CrossRef](#)]
21. Siemens-Dokumentation:imcenter Nastran 2020.1 Help. Available online: https://docs.plm.automation.siemens.com/tdoc/scnastran/2020_1/help/#uid:index (accessed on 20 November 2023).
22. Shampine, L.F.; Reichelt, M.W. The matlab ode suite. *SIAM J. Sci. Comput.* **1997**, *18*, 1–22. [[CrossRef](#)]
23. Schewe, M.; Rembe, C. Signal Diversity for Laser-Doppler Vibrometers with Raw-Signal Combination. *Sensors* **2021**, *21*, 998. [[CrossRef](#)] [[PubMed](#)]

Disclaimer/Publisher's Note: The statements, opinions and data contained in all publications are solely those of the individual author(s) and contributor(s) and not of MDPI and/or the editor(s). MDPI and/or the editor(s) disclaim responsibility for any injury to people or property resulting from any ideas, methods, instructions or products referred to in the content.